Hierarchical single-ion anisotropies in spin-1 Heisenberg antiferromagnets on the honeycomb lattice

Nils Caci, Lukas Weber, and Stefan Wessel

Institute for Theoretical Solid State Physics, RWTH Aachen University, JARA Fundamentals of Future Information Technology, and JARA Center for Simulation and Data Science, 52056 Aachen, Germany

(Received 21 July 2021; revised 21 September 2021; accepted 4 October 2021; published 22 October 2021)

We examine the thermal properties of the spin-1 Heisenberg antiferromagnet on the honeycomb lattice in the presence of an easy-plane single-ion anisotropy as well as the effects of an additional weak in-plane easy-axis anisotropy. In particular, using large-scale quantum Monte Carlo simulations, we analyze the scaling of the correlation length near the thermal phase transition into the ordered phase. This allows us to quantify the temperature regime above the critical point in which—in spite of the additional in-plane easy-axis anisotropy—characteristic easy-plane physics, such as near a Berezinskii-Kosterlitz-Thouless transition, can still be accessed. Our theoretical analysis is motivated by recent neutron scattering studies of the spin-1 compound $BaNi_2V_2O_8$ in particular, and it addresses basic quantum spin models for generic spin-1 systems with weak anisotropies, which we probe over the full range of experimentally relevant correlation length scales.

DOI: 10.1103/PhysRevB.104.155139

I. INTRODUCTION

In recent years, the search for solid-state realizations of Berezinskii-Kosterlitz-Thouless (BKT) topological phase transitions [1–3] in magnetic compounds has lead to the identification of several quasi-two-dimensional (2D) antiferromagnetic candidate materials [4–9]; for an overview over the earlier literature on magnetic compounds for which BKT transitions have been considered, cf. Ref. [10]. While in most systems the BKT behavior is obstructed by the presence of residual interlayer couplings, these were found to be negligible for the specific Ni^{2+} based compound $BaNi_2V_2O_8$, in which spin-1 degrees of freedom reside in effectively decoupled 2D honeycomb lattice layers [11,12]. Instead of interlayer coupling, a weak easy-plane single-ion anisotropy stabilizes dominant planar (XY) correlations in $BaNi_2V_2O_8$ upon lowering the temperature below about 80 K [12]. It was found in theoretical studies that weakly anisotropic 2D Heisenberg antiferromagnets indeed exhibit a vortex-driven BKT transition at a temperature $T_{\rm BKT}$ set by the Heisenberg exchange coupling, separating a disordered high-temperature regime from a quasi-long-range ordered phase below $T_{\rm BKT}$ [13].

However, $BaNi_2V_2O_8$ features a true antiferromagnetic ordering transition [11] at a Néel temperature $T_{\rm N}$ of about 47.75 K [14]. Detailed inelastic neutron scattering studies of the low-temperature ordered state of $BaNi_2V_2O_8$ furthermore indicate the presence of an additional, though very weak, anisotropy which favors the alignment of the magnetic moments along only a subset of directions within the spin's easy plane [12].

As a most basic model system for the magnetism of $BaNi_2V_2O_8$, which accounts for these essential properties [12,14], we consider here the Hamiltonian

$$H = J \sum_{\langle i,j \rangle} \mathbf{S}_i \cdot \mathbf{S}_j + D_z \sum_i \left(S_i^z\right)^2 - D_x \sum_i \left(S_i^x\right)^2, \qquad (1)$$

in terms of spin-1 degrees of freedom $\mathbf{S}_i$ residing on the sites of a honeycomb lattice with an antiferromagnetic nearest-neighbor exchange constant $J > 0$ (i.e., the first sum extends over all nearest-neighbor bonds). Further (weak) interaction terms, e.g., between next-nearest neighboring spins were considered in Ref. [12] based on a linear spin wave theory modeling. The more basic model H in Eq. (1) was then later found to also account well for the neutron scattering data on $BaNi_2V_2O_8$, with the estimated values of $J = 8.8$ meV, $D_z = 0.099$ meV, and $D_x = 0.0014$ meV [14].

The weak anisotropy $D_z \ll J$, along with an even weaker $D_x < D_z$, indeed entails a hierarchy of single-ion anisotropies: A finite $D_z > 0$ leads to the preferred orientation of the spin moments within the spin-XY plane at low temperatures, while the additional $D_x > 0$ favors their alignment in the spin-X direction. Correspondingly, in the pure easy-plane limit $D_x = 0$, the Hamiltonian H has a residual O(2) symmetry in the spin-XY plane and exhibits a BKT transition at a finite transition temperature $T_{\rm BKT}$ (as quantified in detail below). On the other hand, a finite value of $D_x > 0$ explicitly breaks the spin symmetry of H down to a discrete Z_2 symmetry in the spin-X direction, and in this case the system instead exhibits a 2D Ising ordering transition at a finite Néel temperature $T_{\rm N}$ (also quantified below).

Based on the underlying lattice structure, the in-plane anisotropy in $BaNi_2V_2O_8$ may be argued to exhibit a sixfold symmetry instead of a single in-plane easy-axis direction [14]. Due to the irrelevancy of a Z_6 perturbation at the BKT transition [15], the BKT transition would then not be affected by the weak in-plane anisotropy (in the opposite limit of the classical Z_6-symmetric clock model the transition was instead found to no longer be of BKT type [16]). However, the microscopic models that were derived from the inelastic neutron scattering data contain an explicit Z_2 symmetric in-plane anisotropy, as in Eq. (1), which is a strongly relevant perturbation at the BKT transition. Moreover, it was observed in Ref. [14]

that quantum effects in $BaNi_2V_2O_8$ need to be accounted for in order to quantitatively model the correlations in this compound, even though the underlying thermal physics is dominated by classical fluctuations in the weak anisotropy regime. Therefore, our study focuses on the question, whether for temperatures close to and above T_N, one may still be able to identify in the magnetic correlations characteristic features of the dominant easy-plane anisotropy D_z, i.e., remnants of the BKT physics that govern the magnetism of the quantum spin model in Eq. (1) in the pure easy-plane limit $D_x = 0$.

In fact, it was observed recently that within a finite temperature window above T_N, the magnetic correlation length ξ in $BaNi_2V_2O_8$ exhibits a temperature dependence that fits well to the BKT scaling formula $\xi(T) \propto \exp(b/\sqrt{T - T_{BKT}})$ [3], as compared to conventional power-law scaling [14]. In the above, b is a nonuniversal number, and T_{BKT} defines an (effective) BKT transition temperature, estimated for $BaNi_2V_2O_8$ to be 44.7 K, i.e., T_{BKT} is below T_N. This indicates that the BKT physics of vortex excitations still controls the initial buildup of the magnetic correlations in $BaNi_2V_2O_8$ upon approaching the thermal phase transition, but the underlying BKT transition is preempted by the Néel ordering transition that is induced by the additional weak in-plane anisotropy [14].

Here we assess the above scenario for the case of the effective model Hamiltonian H, which allows us to make direct and quantitative comparisons of the correlation length scaling between the full hierarchical model and the pure easy-plane limit ($D_x = 0$). For this purpose we performed a series of large-scale quantum Monte Carlo (QMC) simulations of the hierarchical Hamiltonian H, using a variant of the stochastic series expansion (SSE) method [17–19]. Having in mind a hierarchy of weak anisotropies that is appropriate for the compound $BaNi_2V_2O_8$, we concentrate here on the regime where $D_x < D_z \ll J$. However, we found that important aspects for the analysis of BKT transitions in spin-1 systems on the honeycomb lattice are not available from previous studies. For this reason we first consider in the following several limits of the Hamiltonian H and related models.

More specifically, in the following Sec. II we first examine the BKT transition of the spin-1 XY model on the honeycomb lattice, in order to set the stage for the later discussion of the hierarchical model H. Then, in Sec. III we concentrate on the pure easy-plane limit ($D_x = 0$) of the Hamiltonian H, and then examine the full hierarchical model in Sec. IV. Final conclusions are then drawn in Sec. V. Important technical aspects of the employed SSE algorithm that are specific to the QMC simulation of the anisotropic Hamiltonian H are provided in the Appendixes. There we also examine in detail the quantum phase transition that emerges in the pure easy-plane model for larger values of D_z. Finally, we provide in the Appendixes also an analysis of the pure easy-axis regime ($D_z = 0$) of the Hamiltonian H, for which we identify an enhanced ordering temperature in the large-D_x regime relative to the classical Blume-Capel limit.

II. THE SPIN-1 XY MODEL

While BKT transitions in several anisotropic quantum spin systems have been studied to a high precision in the past, we are not aware of any detailed study of anisotropic spin-1 systems or even the most basic spin-1 XY model on the honeycomb lattice. Hence, before we examine the full hierarchical Hamiltonian H, we first consider the identification of the BKT transition and the correlation length scaling in the most basic spin-1 honeycomb lattice model that exhibits a BKT transition, i.e., the spin-1 XY model. This model is defined by the Hamiltonian

$$H_{XY} = J \sum_{\langle i,j \rangle} S_i^x S_j^x + S_i^y S_j^y, \tag{2}$$

which has a transverse antiferromagnetically ordered ground state for $J > 0$ on a bipartite lattice, and a transverse ferromagnetic ground state for $J < 0$. On a bipartite lattice, such as the honeycomb lattice, both cases can be related by a sublattice rotation, so that here we need to treat explicitly only one of these cases. We consider the antiferromagnetic case in order to set up the notation in the following to apply also directly to the Hamiltonian H, which also contains an antiferromagnetic exchange interaction.

In the following we consider the honeycomb lattice in terms of a triangular lattice with a two-site unit cell. For the QMC simulations we use finite $L \times L$ rhombi of L^2 unit cells and $N = 2L^2$ spins, taking periodic boundary conditions in both lattice directions. Furthermore, we denote the lattice constant in terms of the distance between neighboring lattice sites by a_0.

A standard means of identifying the BKT transition temperature T_{BKT} in O(2) symmetric systems is based on the behavior of the spin stiffness ρ_S, which is predicted to exhibit a universal jump of $\rho_S = 2\,T_{BKT}/\pi$ at the system's BKT transition temperature T_{BKT} [20]. For the specific case of the XY model considered here, we will denote the BKT transition temperature by T_{BKT}^{XY} in the following. Within the SSE QMC approach ρ_S can be calculated from the spin winding number fluctuations [21,22]

$$\rho_S = \frac{T}{2\,A_{uc}} \left(\langle W_x^2 \rangle + \langle W_y^2 \rangle \right), \tag{3}$$

where W_x and W_y are the total winding numbers in the orthogonal x and y direction, respectively. In order to compare to the universal scaling relation of the stiffness jump in the continuum limit, the winding number fluctuations are normalized by the unit cell area A_{uc} in units of a_0^2, which equals $A_{uc} = \sqrt{3}/2$ for the honeycomb lattice. To extract T_{BKT}^{XY} from finite-size QMC data, we then follow the standard approach of Ref. [23], which is based on the finite-size scaling form [24]

$$\frac{\rho_S\,\pi}{2\,T} = A(T) \left(1 + \frac{1}{2\,\log[L/L_0(T)]} \right) \tag{4}$$

that holds exactly at the transition point with $A(T_{BKT}) = 1$. We fitted this finite-size dependence to the data for different temperatures, using $A(T)$ and $L_0(T)$ as fit parameters. This allows us to accurately estimate the transition temperature, where $A(T_{BKT}) = 1$ holds. Our results from this approach are shown in Fig. 1, and we obtain from this analysis an estimate of $T_{BKT}^{XY}/J = 0.7303(4)$ for the spin-1 XY model on the honeycomb lattice.

As another approach to estimate T_{BKT}^{XY}, we analyze the transverse spin correlation function $C_x(r_{i,j}) = \langle S_i^x S_j^x \rangle$, which

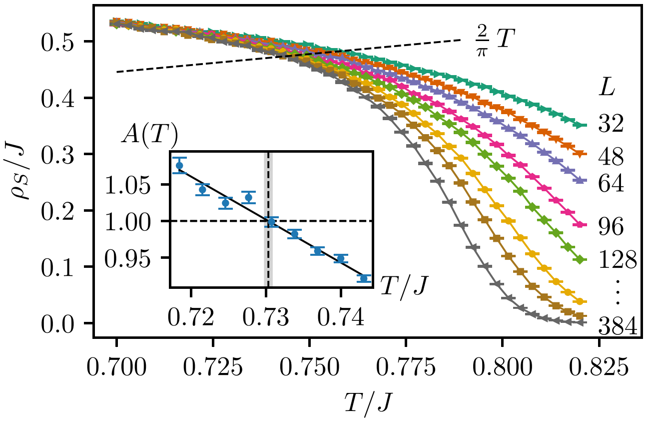

FIG. 1. Spin stiffness ρ_S for different system sizes L as function of temperature T of the spin-1 XY model on the honeycomb lattice. The dashed line denotes the scaling form of the universal jump. The inset shows the quantity $A(T)$ from the finite-size scaling analysis. The critical point is denoted by the dashed vertical line, where $A(T) = 1$ holds, obtained using a linear fit (solid line).

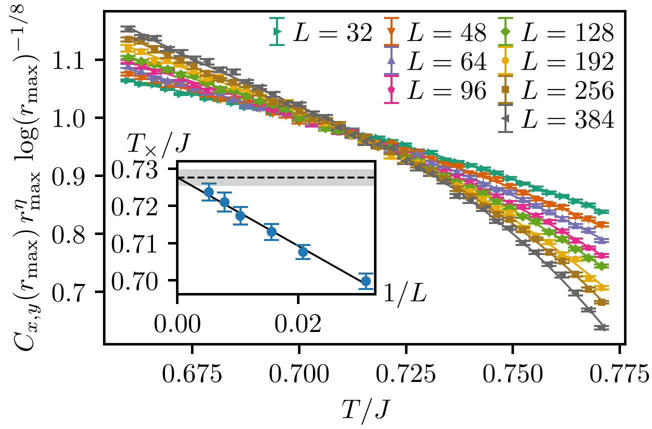

FIG. 2. Transverse spin correlations $C_{x,y}(r_{\max})$, multiplied by $(r_{\max})^{\eta}\,\log(r_{\max})^{-1/8}$ for different system sizes L, as functions of T of the spin-1 XY model on the honeycomb lattice. Near the crossing points they are approximated by polynomials of degree 3 (solid lines). The inset shows the temperature $T_\times$ of the crossing points between the fitting polynomials of linear system sizes L and $2L$ as a function of inverse system size $1/L$, which is extrapolated to $1/L = 0$ using a linear fit (solid line).

for the XY model also equals $C_y(r_{i,j}) = \langle S_i^y S_j^y \rangle$, and where $r_{i,j}$ denotes the spatial distance between spins i and j, accounting for the periodic boundary conditions. In the thermodynamic limit and at the BKT transition temperature, the magnitude $C_{x,y}(r)$ of these correlation functions is predicted to scale as

$$C_{x,y}(r) \sim \frac{\ln(r)^{1/8}}{r^{\eta}}\left[1 + O\left(\frac{\ln(r)^{1/8}}{r^{\eta}}\right)\right], \qquad (5)$$

with the critical exponent $\eta = 1/4$ [25]. We measured the values of $C_{x,y}[r_{\max}(L)]$ at the largest available distance $r_{\max}(L)$ for different lattice sizes L. Based on the above scaling form, we can then estimate $T_{\mathrm{BKT}}^{\mathrm{XY}}$ from a crossing-point analysis of the appropriately rescaled values of $C_{x,y}[r_{\max}(L)]$ between system sizes L and $2L$, and performing an extrapolation to the thermodynamic limit ($1/L = 0$), as shown in Fig. 2. Within the statistical uncertainty, the value $T_{\mathrm{BKT}}^{\mathrm{XY}}/J = 0.728(2)$ that we obtain for the BKT transition temperature from this analysis is in accord with the (more accurate) estimate based on ρ_S reported above.

Following the above identification of the BKT transition temperature in the XY model, we next examine in detail the behavior of the transverse spin correlation length ξ^{XY} in this model and its scaling behavior near $T_{\mathrm{BKT}}^{\mathrm{XY}}$. This analysis will be important to our later study of the scaling behavior of the correlation length in the hierarchical model H.

To extract the correlation length from the spin correlations of a general spin model on the honeycomb lattice, we consider the magnetic structure factor $S_\alpha(\mathbf{q})$, $\alpha = \{x, y, z\}$ defined as

$$S_\alpha(\mathbf{q}) = \tfrac{1}{2}\left[S_\alpha^{AA}(\mathbf{q}) + S_\alpha^{BB}(\mathbf{q}) - S_\alpha^{AB}(\mathbf{q}) - S_\alpha^{BA}(\mathbf{q})\right], \qquad (6)$$

capturing the antiferromagnetic alignment inside the unit cell at $\mathbf{q} = \mathbf{0} = (0, 0)$, where

$$S_\alpha^{\mu\nu}(\mathbf{q}) = \frac{1}{L^2}\sum_{m,n} e^{i\mathbf{q}\cdot(\mathbf{r}_m - \mathbf{r}_n)} C_\alpha^{\mu\nu}(\mathbf{r}_m - \mathbf{r}_n), \qquad (7)$$

with m, n summed over the L^2 unit cells, is given in terms of the correlation function $C_\alpha^{\mu\nu}(\mathbf{r})$ between the α component of two spins at lattice sites belonging to sublattices $\mu, \nu \in \{A, B\}$, and where $\mathbf{r}$ denotes the separation of the unit cells with respect to the underlying triangular lattice. The spin correlation length ξ_α of the fluctuations in the α direction is then obtained in the standard way [26] as

$$\xi_\alpha = \frac{1}{\sqrt{15/16}}\frac{1}{|\mathbf{q}_1|}\sqrt{\frac{S_\alpha(\mathbf{0})}{S_\alpha(\mathbf{q}_1)} - 1}, \qquad (8)$$

where $\mathbf{q}_1$ is one of the reciprocal lattice vectors closest to $\mathbf{0} = (0, 0)$ on the $L \times L$ lattice, and the factor $1/\sqrt{15/16}$ is introduced to relate the estimator to the Ornstein-Zernike correlation length [27].

For the spin-1 XY model we consider the correlation length of the transverse fluctuations $\xi_x = \xi_y$, which we denote by ξ^{XY} in the following. Its temperature dependence is shown in Fig. 3, as obtained from extrapolating the finite-size estimates to the thermodynamic limit (cf. Fig. 4). In this way we are able to reliably extract values of ξ^{XY} up to about 140 lattice constants a_0.

Close to the BKT temperature, the correlation length is predicted to scale as

$$\xi^{\mathrm{XY}} = a \exp\left(b/\sqrt{T - T_{\mathrm{BKT}}^{\mathrm{XY}}}\right), \qquad (9)$$

where a and b are nonuniversal parameters. We find that the numerical data fits well to this BKT scaling form, as shown by the fit line in Fig. 3. In particular, we can also obtain from this analysis a further estimate of $T_{\mathrm{BKT}}^{\mathrm{XY}}/J = 0.7305(3)$, consistent with our previous values. A more direct comparison to the BKT scaling form is obtained by examining ξ^{XY} on a logarithmic scale, for which the BKT scaling form yields

$$\ln(\xi^{\mathrm{XY}}/a_0) = \ln(a/a_0) + b/\sqrt{T - T_{\mathrm{BKT}}^{\mathrm{XY}}}, \qquad (10)$$

which indeed fits well to the numerical data, as seen in the inset of Fig. 3. We thus find that for the spin-1 XY model on

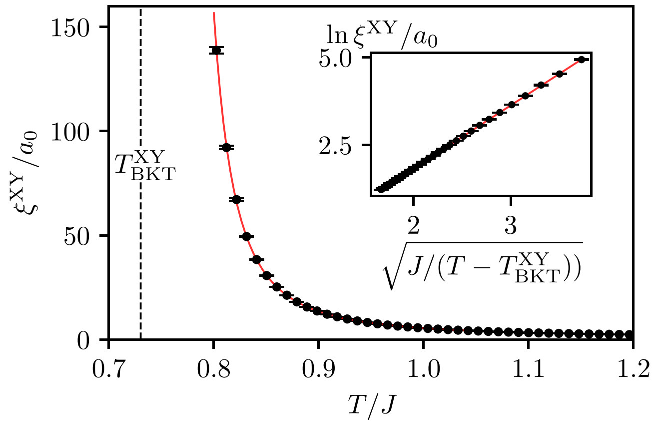

FIG. 3. Correlation length ξ^{XY} of the spin-1 XY model on the honeycomb lattice as a function of T. The solid red line shows a fit to the BKT scaling formula. The inset shows the same data on a logarithmic scale as a function of $1/\sqrt{T - T_{\mathrm{BKT}}^{\mathrm{XY}}}$.

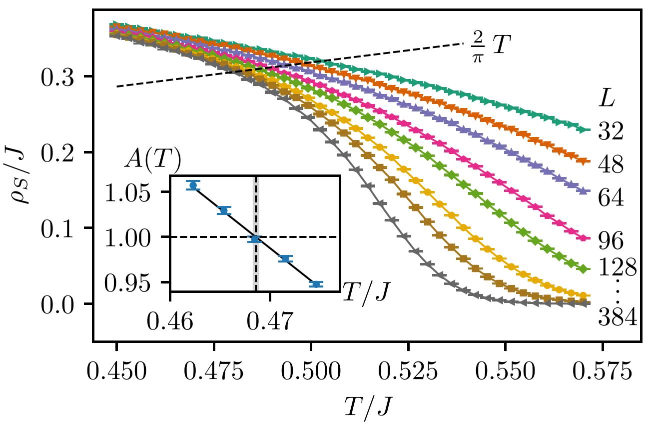

FIG. 5. Spin stiffness ρ_S for different system sizes L as function of temperature T for the spin-1 easy-plane model H_{EP} on the honeycomb lattice for $D_z = 0.01J$. The dashed line denotes the scaling form of the universal jump. The inset shows the quantity $A(T)$ from the finite-size scaling analysis. The critical point is denoted by the dashed vertical line, where $A(T) = 1$ holds, obtained using a linear fit (solid line).

the honeycomb lattice, the correlation length closely follows the BKT scaling form upon approaching the BKT transition temperature.

III. PURE EASY-PLANE REGIME

After having examined the basic spin-1 XY model on the honeycomb lattice, we next turn our attention to the easy-plane limit ($D_x = 0$) of the Hamiltonian H, i.e., we consider

$$H_{\mathrm{EP}} = J \sum_{\langle i,j \rangle} \mathbf{S}_i \cdot \mathbf{S}_j + D_z \sum_i \left(S_i^z\right)^2. \tag{11}$$

Here a finite value of $D_z > 0$ breaks the O(3) symmetry of the Heisenberg model down to a residual O(2) symmetry in the spin-XY plane, and in this two-dimensional model this is expected to lead to a BKT transition in the easy plane, even for very weak anisotropies. As already stated in Sec. I, here we focus on the regime of weak $D_z \ll J$, and we consider in detail the value of $D_z = 0.01J$, which is of the order of the value estimated for $BaNi_2V_2O_8$ [12,14]. In this regime the model indeed exhibits an XY ordered antiferromagnetic ground state and a BKT transition into the low-T critical regime. In the following we first identify the emergence of the BKT transition for the easy-plane spin-1 model on the honeycomb lattice and then analyze the correlation length scaling upon approaching the BKT transition temperature.

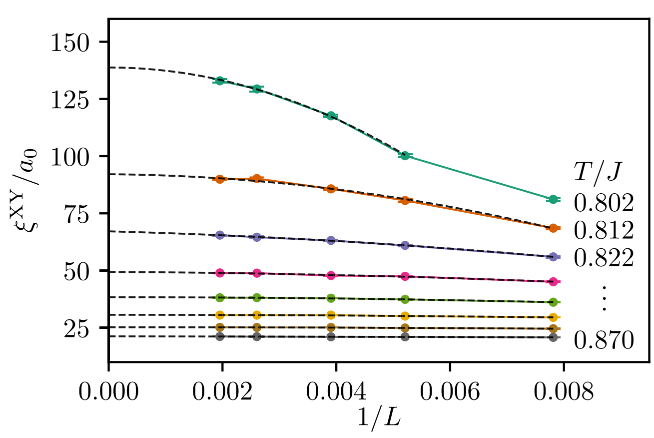

FIG. 4. Extrapolation of the correlation length ξ^{XY} of the spin-1 XY model on the honeycomb lattice from the finite-size data for the lower temperatures from Fig. 3, as obtained from fitting to polynomials of order 2 (dashed lines).

We identity the BKT transition temperature using the spin stiffness ρ_S, following the same approach as introduced in Sec. II. The result of this analysis for H_{EP} is shown in Fig. 5, from which we extract the value of $T_{\mathrm{BKT}}^{\mathrm{EP}}/J = 0.46860(1)$ (we verified that this estimate is also in accord with a corresponding analysis of the correlation function $C_{x,y}[r_{\max}(L)]$, as for the spin-1 XY model in the previous section).

The above procedure can be repeated for varying values of D_z in order to obtain a thermal phase diagram of the Hamiltonian H_{EP}. For completeness we present the QMC data for $T_{\mathrm{BKT}}^{\mathrm{EP}}$ as a function of D_z in Fig. 6. These results exhibit several noticeable features: (i) as a function of D_z, $T_{\mathrm{BKT}}^{\mathrm{EP}}$ exhibits a nonmonotonous behavior: The initial increase of $T_{\mathrm{BKT}}^{\mathrm{EP}}$ with D_z near the isotropic limit is followed by a reduction of $T_{\mathrm{BKT}}^{\mathrm{EP}}$ for $D_z \gtrsim 1$. (ii) $T_{\mathrm{BKT}}^{\mathrm{EP}}$ vanishes for D_z approaching the value of $D_z^c \approx 3.8J$. In fact, as examined in more detail in Appendix B, the Hamiltonian H_{EP} features a quantum phase transition within the three-dimensional (3D) XY universality class at $D_z^c/J = 3.83805(5)$, beyond which the XY-ordered antiferromagnetic ground state gets replaced by a nonmagnetic state due to the proliferation of the local $S_i^z = 0$ states for larger values of D_z. This quantum phase transition was also recently identified within a mean field approximation [28], as well as by QMC for H_{EP} on a square lattice geometry [29]. (iii) The maximum value of $T_{\mathrm{BKT}}^{\mathrm{EP}}$, for $D_z \approx J$, is remarkably close to the value of the BKT transition in the spin-1 XY model H_{XY} (indicated by the horizontal line in Fig. 6). (iv) In the low-D_z regime, we observe an approximate logarithmic suppression

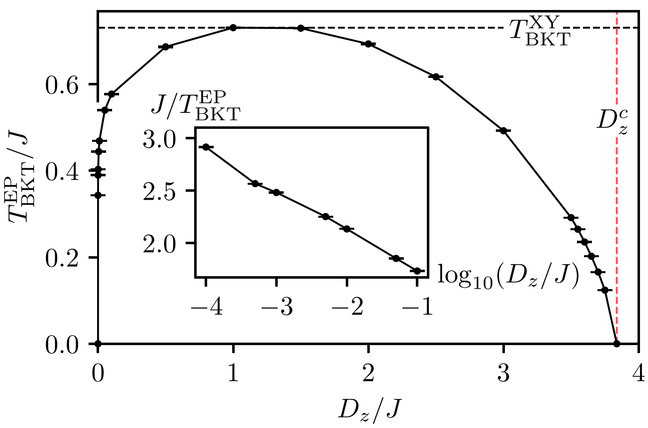

FIG. 6. BKT transition temperature $T_{\rm BKT}^{\rm EP}$ of $H_{\rm EP}$ as a function of the easy-plane anisotropy D_z. The dashed vertical line denotes D_z^c and the dashed horizontal line the BKT transition temperature $T_{\rm BKT}^{\rm XY}$ of $H_{\rm XY}$. The inset indicates the logarithmic scaling of $1/T_{\rm BKT}^{\rm EP} \propto \ln(D_z/c)$ at small D_z.

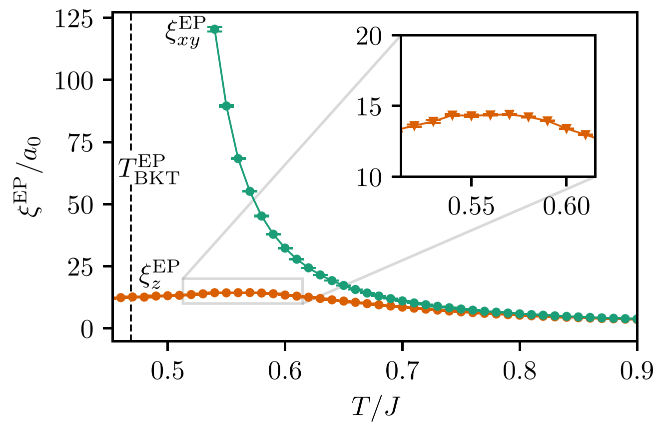

FIG. 7. Correlation lengths $\xi_{xy}^{\rm EP}$ and $\xi_z^{\rm EP}$ as functions of temperature T of the spin-1 easy-plane $H_{\rm EP}$ model on the honeycomb lattice for $D_z = 0.01J$.

of $T_{\rm BKT}^{\rm EP}$, i.e.,

$$T_{\rm BKT}^{\rm EP} \propto 1/\ln(D_z/c), \tag{12}$$

where c is a (nonuniversal) constant (cf. the inset of Fig. 6). Such a leading logarithmic scaling was indeed obtained by earlier spin-wave theory and renormalization group calculations [30,31], and was also observed in numerical studies of both classical and spin-1/2 weakly anisotropic easy-plane XXZ models [13].

For the easy-plane model $H_{\rm EP}$, the correlation lengths ξ_x and ξ_y diverge upon approaching $T_{\rm BKT}^{\rm EP}$. Both quantify the transverse correlations and equal each other due to the residual O(2) symmetry. We thus denote this quantity by $\xi_{xy}^{\rm EP}$ in the following. We also consider the correlation length ξ_z of the longitudinal fluctuations, which we denote by $\xi_z^{\rm EP}$ correspondingly. Both quantities were obtained as described in the previous section, based on the corresponding spin structure factors.

The evolution of these correlation lengths with T, after an extrapolation to the thermodynamic limit, is shown in Fig. 7. Here we again consider the value of $D_z = 0.01J$. In addition to the expected increase of the transverse correlation length $\xi_{xy}^{\rm EP}$, we observe a nonmonotonous behavior in the longitudinal correlation length $\xi_z^{\rm EP}$: For temperatures larger than $T \approx 0.75J$, both correlation lengths closely follow each other, as expected from the O(3) symmetry of the leading Heisenberg exchange term in $H_{\rm EP}$. Below this scale however, $\xi_{xy}^{\rm EP}$ starts to deviate noticeably from $\xi_z^{\rm EP}$. Indeed, $\xi_z^{\rm EP}$, while initially still increasing upon lowering T, exhibits a broad maximum at a temperature T_p of about $T_p \approx 0.56J$ (see the inset in Fig. 7), before it decreases slightly upon further lowering T. In earlier studies of spin-1/2 XXZ models on square lattice geometries, similar behavior of the correlation lengths was observed in the regime of (weak) easy-plane exchange anisotropy [32]. There, the temperature of the maximum in the longitudinal correlation length was identified as a crossover scale separating the high-T Heisenberg region from an intermediate temperature regime with enhanced in-plane fluctuations above the BKT transition.

Returning to $H_{\rm EP}$, at about the crossover scale T_p, the further increase of the transverse correlation length $\xi_{xy}^{\rm EP}$ upon approaching the BKT transition indeed starts to be well described in terms of the exponential BKT scaling of Eq. (9), with $T_{\rm BKT}^{\rm XY}$ replaced by $T_{\rm BKT}^{\rm EP}$. This is illustrated by the fits to the BKT scaling form in Fig. 8. The main panel of Fig. 8 shows the inverse transverse correlation length $a_0/\xi_{xy}^{\rm EP}$ (in units of a_0), which conveniently approaches the value of zero at the BKT transition, along with a fit to the BKT scaling form (unfortunately, due to restrictions in the accessible system sizes, we were not able to explicitly follow this quantity to even lower temperatures than those shown in Fig. 8). The inset of Fig. 8 provides the same data on a logarithmic scale in order to more explicitly demonstrate the approach to a linear scaling of $\ln(a_0/\xi_{xy}^{\rm EP})$ with $1/\sqrt{T - T_{\rm BKT}^{\rm EP}}$, cf. Eq. (10), upon approaching $T_{\rm BKT}^{\rm EP}$. Based on our large-scale QMC simulations, we are thus able to access the correlation length scales

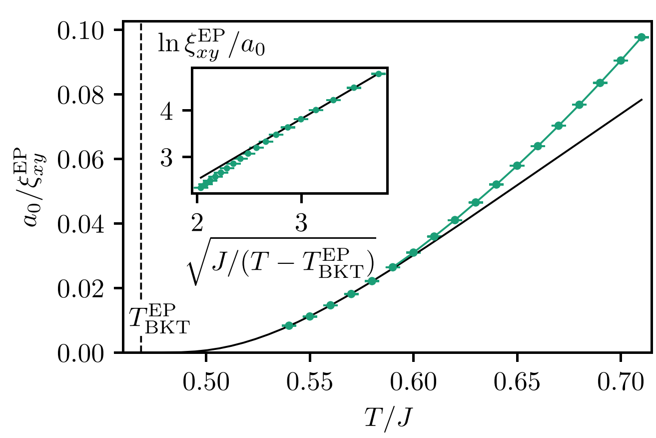

FIG. 8. Inverse correlation length $a_0/\xi_{xy}^{\rm EP}$ of the easy-plane model $H_{\rm EP}$ for $D_z = 0.01J$ as a function of temperature in the vicinity of the BKT transition. The solid black line is a fit of the exponential BKT scaling form to the lowest five data points. The inset shows the same data on a logarithmic scale as a function of $1/\sqrt{T - T_{\rm BKT}^{\rm EP}}$.

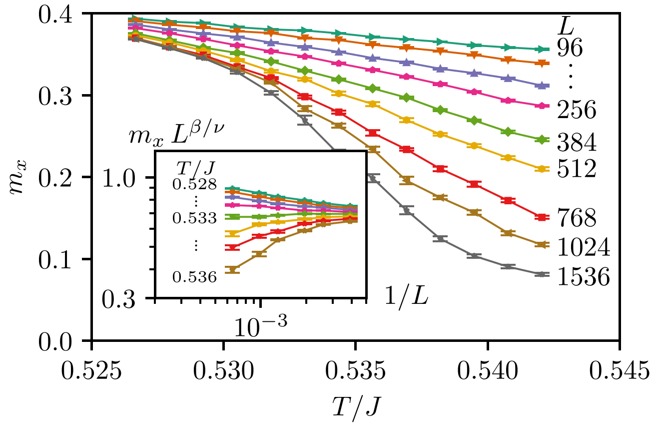

FIG. 9. Order parameter estimator m_x as a function of temperature T for $D_z = 0.01J$, $D_x = 0.1D_z$ for different system sizes L near the antiferromagnetic ordering transition. The inset shows a finite-size scaling plot to estimate T_N, based on the values $\beta = 1/8$ and $\nu = 1$ for the 2D Ising universality class [33].

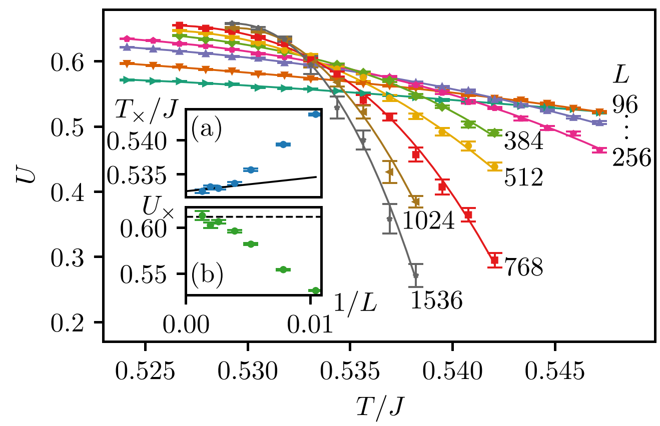

FIG. 10. Binder cumulant U as a function of temperature T for $D_z = 0.01J$, $D_x = 0.1D_z$ for different system sizes L near the antiferromagnetic ordering transition. Close to the crossing points polynomials of degree 3 are used to interpolate the data (solid lines). Inset (a) shows the temperature $T_\times$ of the crossing points between the fitting polynomials of linear system sizes L and $2L$ as functions of the inverse system size $1/L$, extrapolated to the thermodynamic limit using a linear fit (solid line). Inset (b) shows the value of the Binder cumulant $U_\times$ at the crossing points as a function of $1/L$. The critical value U_c of the Binder cumulant for an Ising transition on the triangular lattice is denoted by the dashed line.

that are required in order to observe the onset of BKT scaling of the in-plane correlation length upon approaching the BKT transition of H_{EP}, even for such a weak value of $D_z = 0.01J$ as relevant for the compound $BaNi_2V_2O_8$ [12,14].

In the next section we will examine to what extent this accessibility of the characteristic correlation length scaling near a BKT transition is affected by the additional presence of a finite in-plane easy-axis anisotropy $D_x > 0$ in the full Hamiltonian H.

IV. HIERARCHICAL ANISOTROPIES

After having established the BKT transition in the easy-plane limit, as well as the associated correlation length scaling, we now consider the hierarchical model H with finite values of both anisotropies. Since a finite value of $D_x > 0$ breaks the O(2) symmetry from the easy-plane limit H_{EP} down to a residual Z_2 symmetry in the spin-X direction, the hierarchical model H exhibits a low-T thermal Ising transition to a low-temperature antiferromagnetically ordered state, with a finite value of the staggered magnetization in the spin-X direction. In the following we first focus on the case of $D_x = 0.1D_z$, where $D_z = 0.01J$ as in the previous section. For this value of D_x we are able to examine the thermal phase transition in more detail than for even lower values of D_x (due to the increasingly larger system sizes that are required to observe the asymptotic critical scaling at even lower values of D_x). Later, we also turn to values of $D_x/D_z = 0.01$–0.05, which are more relevant in view of the compound $BaNi_2V_2O_8$ [12,14].

In the QMC simulations we can quantify the emergence of the low-temperature magnetic state in terms of the estimator

$$m_x = \sqrt{\frac{1}{2L^2} S_x(\mathbf{0})} \tag{13}$$

for the absolute value of the staggered magnetization. Figure 9 shows the temperature dependence of m_x for various linear system sizes L, for $D_z = 0.01J$ and $D_x = 0.1D_z$. The temperature range in Fig. 9 focuses on the transition region into the low-T ordered phase, which is seen to emerge in the thermodynamic limit below a Néel temperature of $T_N \approx 0.53J$. As the antiferromagnetic order breaks the residual Z_2 symmetry of H, the thermal phase transition at T_N is expected to belong to the universality class of the 2D Ising model. Using the finite-size scaling $m_x \propto L^{-\beta/\nu}$ at criticality, with the exactly known values $\beta = 1/8$ and $\nu = 1$ for the critical exponents in the 2D Ising universality class [33], we extract $T_N/J = 0.533(1)$, based on an appropriate scaling plot as shown in the inset of Fig. 9.

In order to obtain a more accurate estimate for T_N and to confirm the anticipated Ising model universality class of the phase transition at T_N, we analyze the Binder cumulant [34,35]

$$U = 1 - \frac{1}{3} \frac{\langle m_x^4 \rangle}{\langle m_x^2 \rangle^2}, \tag{14}$$

which is shown in Fig. 10 for different system sizes in the vicinity of T_N. Using a crossing-point analysis of the values of U for system sizes L and $2L$, we can obtain an estimate for the ordering temperature: An extrapolation of the temperatures $T_\times$ of these crossing points to the thermodynamic limit [cf. inset (a) of Fig. 10], gives $T_N/J = 0.5325(1)$. The critical value of the Binder cumulant for the Ising model on triangular lattices with rhombic shapes has previously been determined to $U_c = 0.61182\ldots$ [36,37]. Given the underlying triangular structure of the honeycomb lattice, we expect the critical Binder ratio to agree with this value. We indeed find the data for the Binder cumulants at the crossing points $U_\times$ to approach this value in the thermodynamic limit [cf. inset (b) of Fig. 10]. This is in accord with the expected universality class of the phase transition at T_N. We note that for a controlled extrapolation to the thermodynamic limit we require rather large system sizes, e.g., the crossing points in the Binder ratio in Fig. 10 exhibit significant drifts even for values of L of several hundreds.

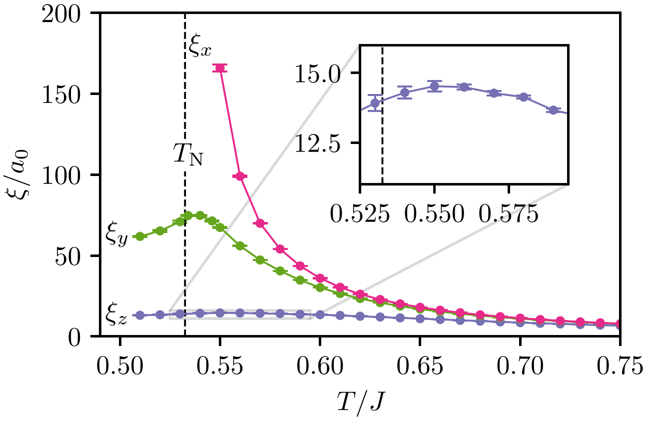

FIG. 11. Correlation lengths ξ_x, ξ_y, and ξ_z as functions of T for $D_z = 0.01J$, $D_x = 0.1D_z$. The dashed line indicates the Néel temperature T_N.

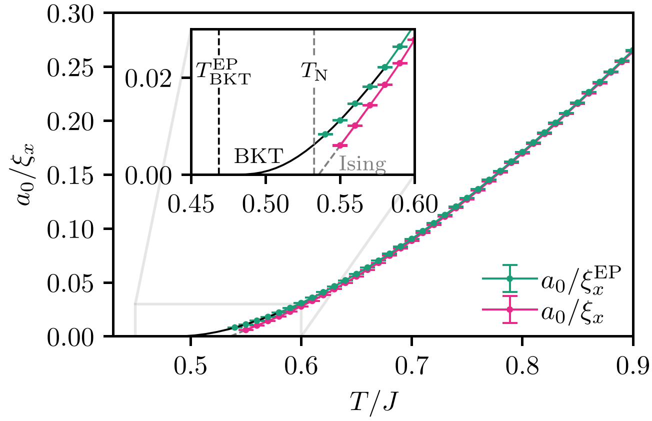

FIG. 12. Inverse correlation length a_0/ξ_x for $D_z = 0.01J$, $D_x = 0.1D_z$ as a function of temperature T, and compared to the inverse correlation length a_0/ξ_x^{EP} of the easy-plane model ($D_x = 0$). The solid line is a fit to the exponential BKT scaling form for ξ_x^{EP}, and the dashed line is an extrapolation of the linear drop in a_0/ξ_x near the Ising transition.

Most importantly, we can confirm from this analysis that the phase transition at T_N belongs to the Ising universality class and thus the BKT transition, which takes place for $D_x = 0$, is replaced by a true ordering transition in the full hierarchical model at finite D_x.

After having established the thermal phase diagram of the hierarchical model, we now turn to analyze the behavior of the correlation lengths in this system. For this purpose we determined the correlation lengths ξ_x, ξ_y, and ξ_z, in all three spin directions, using the approach from Sec. II. Their temperature dependence, after an extrapolation to the thermodynamic limit, is shown in Fig. 11. While for large temperatures the three correlation lengths are very similar, as expected from the O(3) symmetry of the leading Heisenberg exchange term in H, they exhibit noticeable different behavior below about $T \approx 0.75J$. In particular, both in-plane correlation lengths ξ_x and ξ_y exhibit an enhanced further increase, whereas this is less pronounced for ξ_z. Similarly to the easy-plane case in Sec. III, ξ_z instead exhibits only a rather broad maximum at about $T \approx 0.55J$, i.e., slightly above T_N, before its decrease in the ordered phase. We observe that ξ_y still follows the increase of ξ_x down to $T \approx 0.65J$. Within the temperature window $0.65 \lesssim T/J \lesssim 0.75$, the correlations can thus be characterized as easy-plane-like (note that this does not imply BKT scaling within this temperature regime). For even lower temperatures, ξ_y however falls noticeably below ξ_x, and it reaches a maximum at a similar temperature scale as ξ_z, but with a substantially larger maximum value, before it also decreases in the ordered phase in a more noticeable manner. Since ξ_x is the only diverging correlation length in the hierarchical system, we concentrate in the following on the behavior of this dominant correlation length upon approaching the thermal phase transition.

While a finite value of the anisotropy $D_x > 0$ strongly affects the nature of the phase transition and the scaling of the correlation length ξ_x in the low-temperature region, we expect it to be only little affected by the weak value of D_x for temperatures well above T_N. Indeed, we find ξ_x to closely follow ξ_{xy}^{EP} at large temperatures. Upon approaching T_N however, ξ_x deviates increasingly from the easy-plane values ξ_{xy}^{EP}, as shown in Fig. 12, where we again consider the inverse correlation lengths, since they conveniently approach zero at the thermal phase transitions.

Upon lowering the temperature we observe a different behavior in the transverse correlation lengths for the two models: while the data for the easy-plane model approaches the BKT scaling form (indicated by the solid line in Fig. 12), the hierarchical model shows clear deviations from this behavior. Instead, we can identify (cf. the inset) the onset of a linear decrease of a_0/ξ_x, which results from the emergence of the algebraic scaling near the Néel temperature, $\xi_x \propto (T - T_N)^{-\nu}$ of the 2D Ising model universality, i.e., $\nu = 1$. Indeed, the linear extrapolation of the linear drop in a_0/ξ_x, shown in the inset of Fig. 12, yields an upper bound for T_N that is only slightly larger than the previously determined value of T_N, where a_0/ξ_x vanishes.

We thus find that for the value of $D_x = 0.1D_z$ considered so far, the system does not show an extended crossover region separating the anisotropic high-T region from the low-T algebraic scaling of ξ_x due to the onset of the Ising criticality. This situation is expected to change for even smaller value of D_x, since this weakens the effects of the in-plane anisotropy. More quantitatively, in Fig. 13 we compare the behavior of the correlation length ξ_x for varying values of D_x, as obtained from QMC simulations. We indeed find that (i) for the lower two values of D_x, the data follows more closely the behavior of the easy-plane model towards lower temperatures, and (ii) for these lower values of D_x, we can identify an intermediate temperature regime in which the correlation length growth for the hierarchical model follows the BKT scaling prior to the onset of the asymptotic Ising scaling. More quantitatively, one can introduce an effective BKT transition temperature T_{BKT}^* (denoted T_{BKT} in Ref. [14]), such that the intermediate growth of ξ_x can be fitted to the scaling in Eq. (9) (with T_{BKT}^{XY} replaced by T_{BKT}^*), prior to the onset of the extrapolated characteristic linear Ising-model scaling of a_0/ξ_x near the ordering transition. For both values of D_x, the extracted values of T_{BKT}^* are smaller than the estimated values of T_N, in accord with the

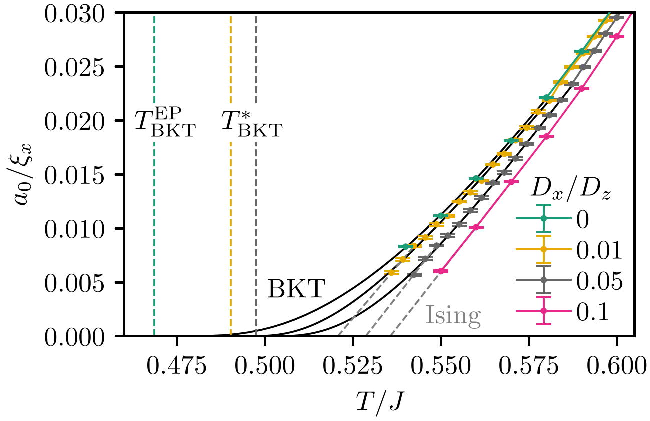

FIG. 13. Inverse correlation length a_0/ξ_x for $D_z = 0.01J$ and different values of D_x as functions of temperature T, and compared to the inverse correlation length $a_0/\xi_x^{\rm EP}$ of the easy-plane model with $D_x = 0$. Solid black lines are fits to the exponential BKT scaling form, and dashed lines extrapolations of the linear drop in a_0/ξ_x near the Ising transition.

interpretation that the BKT transition in the easy-plane limit is preempted by the onset of Néel order, due to the finite value of D_x in the full Hamiltonian H. Accordingly, upon lowering D_x, the value of $T_{\rm BKT}^*$ also approaches closer to the true BKT transition temperature $T_{\rm BKT}^{\rm EP}$ of the easy-plane limit.

Finally, we consider the estimation of the Néel temperature for the lower values of D_x. As we already mentioned, it is not feasible to accurately determine $T_{\rm N}$ for these lower values of D_x based on the analysis of the Binder cumulant that we performed for $D_x/D_z = 0.1$, since inaccessibly large system sizes would be required for such an approach. One could then try to estimate $T_{\rm N}$ from the linear extrapolations shown in Fig. 13. However, these extrapolations provide only an upper bound on $T_{\rm N}$, similar to what we observed already for the case of $D_x/D_z = 0.1$ in Fig 12. In fact, we expect that even lower temperatures (and therefore also larger system sizes due to the further increasing correlation length) are necessary in order to reach the asymptotic Ising scaling regime for ξ_x and to reliably extract $T_{\rm N}$ from the extrapolation of the correlation length data for these low values of D_x. In view of this limitation, it would certainly be interesting to quantify the actual D_x dependence of $T_{\rm N}$ based on other, analytical treatments such as renormalization group calculations.

V. CONCLUSIONS

We examined the thermal properties of anisotropic spin-1 Heisenberg antiferromagnets on the honeycomb lattice, with a focus on the behavior of the correlation length near the thermal phase transition. For this purpose we first considered both the basic XY model and the pure single-ion anisotropic easy-plane model. For both systems we determined the value of the BKT transition temperature and also explored its D_z dependence for the easy-plane case. Furthermore, we confirmed that the correlation-length growth in the easy-plane case approaches the BKT scaling form upon approaching the BKT transition temperature. For the XY model the BKT scaling is even observed up to temperatures at which the correlation length becomes of the order of the lattice constant.

In addition, we considered the effects of a weak additional in-plane easy-axis anisotropy, which breaks the O(2) symmetry of the pure easy-plane model down to a residual Z_2 symmetry. This provides us with a basic quantum spin model for examining the situation in the Ni^{2+} based compound $BaNi_2V_2O_8$. We were able to explicitly demonstrate the onset of Ising criticality for such a hierarchical model with two different single-ion anisotropies. However, we also found that for sufficiently weak values of the easy-axis anisotropy, as reported for $BaNi_2V_2O_8$ [12], one can still identify a narrow temperature regime above the Néel ordering temperature, in which the critical correlation length follows the characteristic BKT scaling form in terms of an effective BKT transition temperature $T_{\rm BKT}^*$, which lies between the Néel ordering temperature and the BKT transition temperature of the easy-plane limit.

Returning to the case of $BaNi_2V_2O_8$, for which an extended BKT scaling regime was reported recently in the correlation length [14], our results confirm that the characteristic BKT scaling of the correlation length can be identified in the hierarchical model of the magnetism in this compound on length scales of the order of a hundred lattice constants. It would of course be important to more accurately quantify the width of this intermediate BKT scaling regime in terms of the hierarchical anisotropies. In addition, it would be interesting to take the discrete lattice symmetries of $BaNi_2V_2O_8$ into account in the microscopic modeling [12], replacing thereby the residual Z_2 symmetry of H by a Z_6 symmetry [14], which is expected to further stabilize the BKT transition and its corresponding scaling regime [15].

ACKNOWLEDGMENTS

We acknowledge insightful discussions with Bella Lake, Ekaterina Klyushina, and Johannes Reuther, as well as support by the Deutsche Forschungsgemeinschaft (DFG) through Grant No. WE/3649/4-2 of the FOR 1807 and through RTG 1995, and thank the IT Center at RWTH Aachen University and the JSC Jülich for access to computing time through the JARA Center for Simulation and Data Science.

APPENDIX A: STOCHASTIC SERIES EXPANSION

The stochastic series expansion QMC method with directed loop updates [17–19,38] offers an unbiased approach to study sign-free quantum spin systems. In the following we comment on some technical aspects that are relevant for the SSE simulations of the specific models that we considered here. For a more general and detailed introduction, cf., e.g., Ref. [19].

The starting point of the SSE QMC method is a high temperature expansion of the partition function

$$Z = \mathrm{Tr}(e^{-\beta H}) = \sum_\alpha \sum_{n=0}^{\infty} \frac{\beta^n}{n!} \langle\alpha|\,(-H)^n\,|\alpha\rangle\,, \qquad \text{(A1)}$$

where $\{|\alpha\rangle\}$ is a orthonormal basis of the Hilbert space of H, called the computational basis. Here we use the standard local product S^z basis, i.e., $|\alpha\rangle = |S_1^z, S_2^z, \dots, S_N^z\rangle$. To evaluate the matrix elements $\langle\alpha|\,(-H)^n\,|\alpha\rangle$, the Hamiltonian H is decomposed as $H = -\sum_{b,t} H_{b,t}$ into a sum of bond operators $H_{b,t}$, specified by a bond index b, and the operator type t. These bond operators must be nonbranching, i.e., the action of $H_{b,t}$ on a given basis state $|\alpha\rangle$ is proportional to another basis state $|\alpha'\rangle$. Introducing a sequence of bond operators $S_n = \{[b_1, t_1], \ldots, [b_n, t_n]\}$ that contributes to the partition function, we can rewrite Z as

$$Z = \sum_{\alpha}\sum_{n=0}^{\infty}\sum_{\{S_n\}} \frac{\beta^n}{n!} \langle\alpha|\prod_{i=1}^{n}(H_{b_i,t_i})\,|\alpha\rangle\,, \qquad \text{(A2)}$$

where the expansion order n corresponds to the number of operators in S_n, i.e., its length. In practice, the expansion order is fixed to some cut-off L that is set larger than the maximally sampled expansion order. In this fixed length representation the operator string S_L is padded with unity operators, such that n corresponds to the number of nonunity operators in S_L. The expansion order n, the state $|\alpha\rangle$, as well as the operators in the string S_L are then sampled during the Monte Carlo updating procedures.

In the diagonal update step operators that are diagonal in the computational basis are inserted or removed from S_L. The second update step is the directed-loop update, which is a global update that proceeds via locally constructing a cluster of operators in S_L, viewed as list of vertices along with two incoming and outgoing legs. The latter carry the local spin state of the two sites that belong to the bond b of the bond operator. If the matrix elements of the diagonal operators are much larger than those of the off-diagonal operators, these local steps during the (global) directed-loop update each have very low acceptance probabilities. This can cause the updating dynamics to freeze and may lead to ergodicity problems of the Monte Carlo update.

After these general remarks, we consider the hierarchical Hamiltonian H, i.e.,

$$H = J\sum_{\langle i,j\rangle}\mathbf{S}_i\cdot\mathbf{S}_j + D_z\sum_i\left(S_i^z\right)^2 - D_x\sum_i\left(S_i^x\right)^2, \qquad \text{(A3)}$$

and we first examine the decomposition into bond operators. In the following we consider a bond b connecting the two sites i and j on the honeycomb lattice. The decomposition leads to three types of bond operators $H_{b,t}$, $t = 0, 1, 2$, which are classified by the action on the spins connected by this bond: (i) a bond operator that is diagonal in the computational basis,

$$H_{b,0} = C - JS_i^zS_j^z - \sum_{k\in\{i,j\}}\left(\frac{D_z}{z}\left(S_k^z\right)^2 - \frac{D_x}{4z}\left(S_k^+S_k^- + S_k^-S_k^+\right)\right), \qquad \text{(A4)}$$

where an appropriate constant C can be added in order to ensure that all matrix elements are positive, (ii) a first off-diagonal part due to the Heisenberg exchange,

$$H_{b,1} = -\frac{J}{2}\left(S_i^+S_j^- + S_i^-S_j^+\right), \qquad \text{(A5)}$$

as well as (iii) a second off-diagonal part due to the easy-axis anisotropy D_x,

$$H_{b,2} = \frac{D_x}{4z}\sum_{k\in\{i,j\}}\left(S_k^+S_k^+ + S_k^-S_k^-\right). \qquad \text{(A6)}$$

Here $z = 3$ is the coordination number on the honeycomb lattice. The full Hamiltonian is given by the sum $H = N_bC - \sum_{b,t} H_{b,t}$ over these bond operators (N_b denotes the number of bonds on the finite lattice). On a bipartite lattice, such as the honeycomb lattice considered here, all finite contributions to the partition function in Eq. (A2) have positive weights, and can thus be sampled without a sign problem.

Several observations are in order: (i) For finite values of D_x, the presence of the bond operator $H_{b,2}$ leads to the following modification from the standard directed loop update: the head of the moving operator, which is assigned a local S^+ or S^- operator, is now allowed to switch-and-revert [19] to the other site of a local vertex without being inverted. (ii) The easy-axis anisotropy D_x contributes to both the diagonal and off-diagonal operators, whereas the easy-plane anisotropy D_z contributes only to diagonal operators. In the limit of large $|D_z|$, this leads to sampling problems, which result in larger statistical errors. We observed that these are reduced, if the larger of the two anisotropies aligns in the spin-X direction. For this purpose, one can perform a rotation of the Hamiltonian in the spin plane about the spin-Y axis, without introducing a QMC sign problem due to the bipartiteness of of the honeycomb lattice. (iii) Some observables, in particular the Binder ratio U, are more readily accessible after performing such a rotation of the Hamiltonian about the spin-Y axis. Indeed, the second and forth moments of the the order parameter are then diagonal observables in the computational basis. For our simulations, we took those observations into account in order to optimize the computational efforts.

APPENDIX B: QUANTUM PHASE TRANSITION IN THE PURE EASY-PLANE MODEL

In this Appendix we examine the high-D_z continuous quantum phase transition of the spin-1 easy-plane Hamiltonian

$$H_{\mathrm{EP}} = J\sum_{\langle i,j\rangle}\mathbf{S}_i\cdot\mathbf{S}_j + D_z\sum_i\left(S_i^z\right)^2 \qquad \text{(B1)}$$

in more detail. In addition to breaking the SO(3) symmetry of the Heisenberg model, finite values of $D_z > 0$ suppress the local spin states $S_i^z = \pm 1$, whereas the local state $S_i^z = 0$ is preferred by finite $D_z > 0$. In the large-D_z limit, the ground state is given by the direct product state $|0\rangle = \prod_i |S_i^z = 0\rangle$, with $S_i^z = 0$ on each lattice site i. We expect a quantum phase transition to take place at a finite value of $D_z > 0$, beyond which the XY-antiferromagnetic ground state gets replaced by a nonmagnetic state that connects to this large-D_z limit product state. To gain insight into this transition, we can employ a simple perturbative argument in the limit $J/D_z \ll 1$: The energy spectrum of the unperturbed Hamiltonian $H^{(0)} = D_z\sum_i(S_i^z)^2$ in this limit is described by the number of local $S_i^z = \pm 1$ states, which we denote by $N_\pm$. It is therefore given by the discrete energies $E^{(0)}_{N_\pm} = D_zN_\pm$, which are well separated from each other. The direct product state $|0\rangle$ is the ground state of $H^{(0)}$, with $E^{(0)}_0 = 0$. The lowest excited states belong to the $N_\pm = 1$ sector, with $E^{(0)}_1 = D_z$. In contrast to the ground state $|0\rangle$, this energy level is thus highly degenerate. The Heisenberg exchange interaction allows a local $S_i^z = \pm 1$ excitation atop the state $|0\rangle$ to hop on the honeycomb lattice. This leads to an effective tight-binding kinetic energy contribution, with a hopping amplitude that is equal to J on the honeycomb lattice. This results into a J-dependent change of the lowest excitation energy in the $N_\pm = 1$ sector to $E_1^{(0)} + E_1^{(1)} = D_z - 3J$ on the threefold coordinated honeycomb lattice within this first-order perturbation theory.

The direct product state $|0\rangle$ in the $N_\pm = 0$ sector instead does not change within first-order perturbation theory. Upon comparing the energies from the two sectors, we thus expect from this lowest-order perturbative calculation a critical value D_z^c of D_z, where a transition takes place out of the large-D_z ground state $|0\rangle$. More specifically, we obtain from this analysis a first-order estimate for the critical easy-plane anisotropy of $D_z^c = 3J$. A more quantitative computation needs to consider also higher-order terms and excited states in the perturbative expansion, which result in a dressing of the ground state $|0\rangle$ for finite values of J/D_z. We furthermore expect those contributions to replace the level-crossing transition from the first-order approach by a continuous quantum phase transition in the thermodynamic limit. Indeed, from symmetry considerations, we expect a continuous quantum phase transition to separate the two regimes, belonging to the three-dimensional O(2) universality class, based on the global O(2) symmetry of the easy-plane Hamiltonian in $d = 2$ spatial dimensions. In addition, the dynamical critical exponent is then equal to $z = 1$. In order to accurately locate the quantum phase transition, we turn to QMC simulations. More specifically, we consider the spin stiffness ρ_S, which scales at the quantum critical point as [26,39–41]

$$\rho_S \propto L^{2-d-z}, \tag{B2}$$

in order to accurately calculate D_z^c. Based on $z = 1$, we measured ρ_S at an inverse temperature of $\beta = 2L$ for different linear system sizes up to $L = 96$ and for different easy-plane anisotropies D_z. The numerical results for ρ_S are shown in Fig. 14. The value of $D_z^c/J = 3.83805(5)$ is then obtained upon extrapolating crossing points in ρ_S from system sizes L and $2L$ to the thermodynamic limit, as indicated by the vertical line in Fig. 14.

The actual value of D_z^c is larger that the above first-order perturbative estimate, which however already provides the right order of magnitude. Also included in Fig. 14 (in the inset) are QMC results for the mean occupation density n_0 of the local $S_i^z = 0$ states. This quantity increases from the exact SU(2)-symmetric value of 1/3 for $D_z = 0$ to the limiting value of 1 in the large-D_z limit. Furthermore, it evolves smoothly across the quantum phase transition (as befits a continuous transition), merely exhibiting a mild kink at the quantum critical point.

Near the quantum critical point at D_z^c, the BKT transition temperature is expected to scale as

$$T_{\mathrm{BKT}}^{\mathrm{EP}} \propto \left(D - D_z^c\right)^{\nu z}, \tag{B3}$$

where $\nu = 0.67155(27)$ for the 3D XY model [42]. As shown in Fig. 15, our numerical results for $T_{\mathrm{BKT}}^{\mathrm{EP}}$ are in accord with an approach to this scaling close to D_z^c.

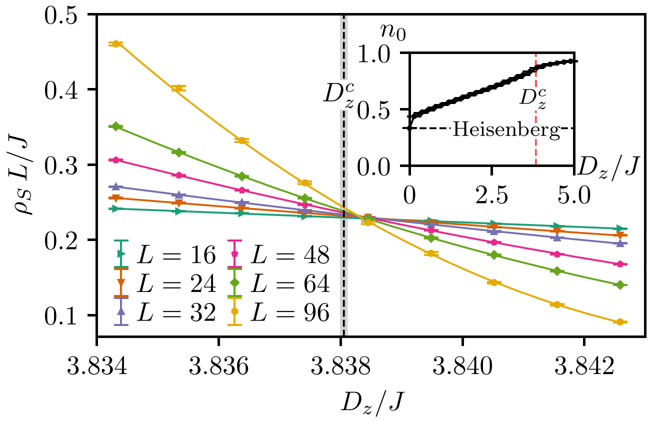

FIG. 14. Spin stiffness ρ_S multiplied by L at $\beta = 2L$ as a function of D_z of the spin-1 easy-plane model H_{EP} on the honeycomb lattice of different linear system size L. Polynomials of degree 3 are used to interpolate the data (solid lines). The critical value D_z^c, obtained by extrapolating the crossing points of the fitting polynomials in $\rho_S L$ for system sizes L and $2L$, is denoted by the (dashed) vertical line. The inset shows the mean occupation density n_0 of the local $S_i^z = 0$ states as a function of D_z (for $L = 48$, $\beta = 2L$). The vertical line denotes D_z^c, while the horizontal lines indicates the occupation density of the spin-1 Heisenberg model.

APPENDIX C: PURE EASY-AXIS MODEL

In this Appendix we examine the pure easy-axis regime ($D_z = 0$) of the Hamiltonian H. Moreover, we also introduce an exchange anisotropy in the form of the additional parameter λ, such that we consider here the Hamiltonian

$$H_{\mathrm{EA}} = J \sum_{\langle i,j\rangle} S_i^x S_j^x + \lambda\left(S_i^y S_j^y + S_i^z S_j^z\right) - D_x \sum_i \left(S_i^x\right)^2, \tag{C1}$$

which for $\lambda = 1$ recovers the original Heisenberg interaction of H, while in the limit $\lambda = 0$ a classical spin model is obtained. This classical limit of our spin-1 model is the well known Blume-Capel model [43,44]. Both models are usually formulated in terms of the spin-Z direction as the easy axis

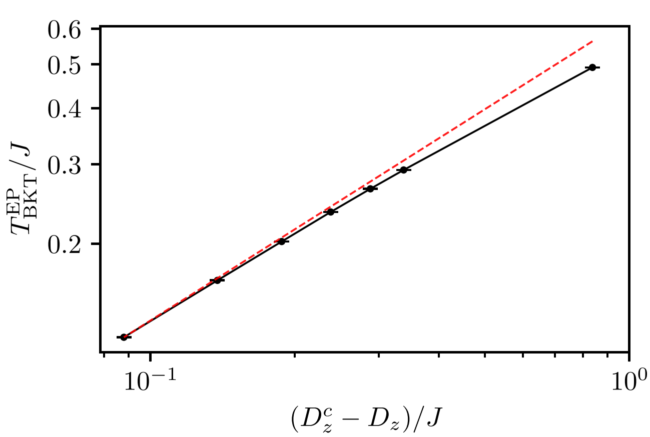

FIG. 15. BKT transition temperature of the spin-1 easy-plane model H_{EP} on the honeycomb lattice in the vicinity of the quantum critical point in a log-log plot, compared to the scaling prediction in Eq. (B3) near D_z^c, indicated by the slope of the dashed line.

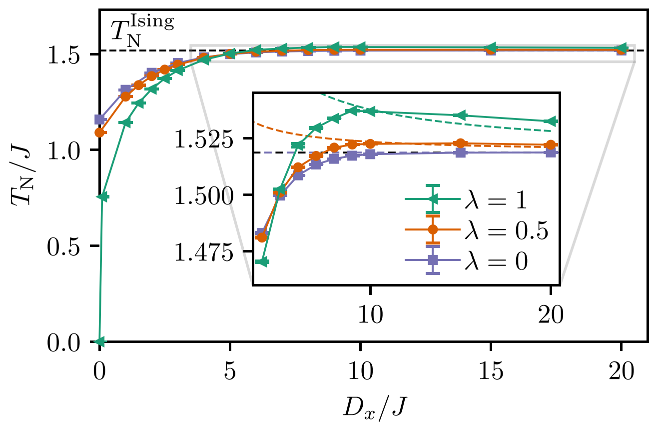

FIG. 16. Néel temperature T_N as a function of the easy-axis anisotropy D_x in H_{EA} for different values of λ. The dashed lines denote results from second-order Brillouin-Wigner perturbation theory in the large D_x limit.

instead of the spin-X direction, which we use here in order to remain consistent with our convention in the main part of the paper.

As in the full hierarchical model H, a finite value of $D_x > 0$ leads to a thermal phase transition into a low-T phase with antiferromagnetic order in the spin-X direction. We can obtain the corresponding Néel temperature T_N from QMC simulations based on the Binder cumulant analysis as discussed in Sec. IV (for $\lambda = 0$, we used the approach of Ref. [45] to simulate the Blume-Capel model). The results for T_N for different values of λ are summarized in Fig. 16.

Let us first consider the classical (Blume-Capel) limit $\lambda = 0$. Here, for large values of D_x, the Néel temperature approaches the value of the two-dimensional Ising model (on the honeycomb lattice), which is known exactly and equal to $T_N^{\rm Ising}/J = 1.518\ldots$ [46]. Indeed, a large value of D_x suppresses the local spin states $S_i^x = 0$ (in the spin-X basis), whereas the local spin states $S_i^x = \pm 1$ are energetically favorable. As a result, for $\lambda = 0$, due to the $S_i^x S_j^x$ term in the exchange coupling, we (exactly) obtain an Ising model in the limit $D_x \to \infty$.

Turning now to the case of nonzero $\lambda > 0$, we find that again the Néel temperature tends towards the Ising model value for large D_x. However, we observe in this case a non-monotonous behavior in the D_x dependence of T_N, as seen in the zoom of Fig. 16. In particular, we find that for finite values of λ, the Néel temperature approaches $T_N^{\rm Ising}$ from above, in contrast to the classical limit ($\lambda = 0$), in which T_N increases monotonously and approaches $T_N^{\rm Ising}$ from below.

To gain analytical insight into this behavior, we investigated the large-D_x region using second-order Brillouin-Wigner perturbation theory to derive an effective Hamiltonian in the large-D_x regime. We find that, up to second order in J/D_x, H_{EA} can be described by a spin-1/2 XXZ model, given by

$$H_{EA}^{\rm eff} = J \sum_{\langle i,j\rangle} -\lambda_{\rm eff}\left(S_i^y S_j^y + S_i^z S_j^z\right) + \Delta S_i^x S_j^x, \qquad \text{(C2)}$$

where

$$\lambda_{\rm eff} = \frac{\lambda^2}{2}\frac{J}{D_x}, \quad \Delta = \left(4 + \frac{\lambda^2}{2}\frac{J}{D_x}\right). \qquad \text{(C3)}$$

The derivation of this effective Hamiltonian can be found in Appendix D.

In terms of the parameters of $H_{EA}^{\rm eff}$, the large-D_x regime corresponds to the limit $\Delta \gg \lambda_{\rm eff}$, in which the Néel temperature of the spin-1/2 XXZ model approaches $\Delta T_N^{\rm Ising}/4$ (cf. also Ref. [47] for a square lattice geometry). From the expression for Δ in Eq. (C3), we thus indeed find that for finite $\lambda > 0$ in the large-D_x regime, the Néel temperature

$$T_N \approx \left(1 + \frac{\lambda^2}{8}\frac{J}{D_x}\right) T_N^{\rm Ising} \qquad \text{(C4)}$$

approaches $T_N^{\rm Ising}$ from above, as observed also in the QMC data. A quantitative comparison between the QMC data and the perturbation theory result is included in Fig. 16. We find that the second-order perturbation theory fits well to the trend seen in the QMC data for increasingly large values of D_x. However, this comparison also reveals that higher-order contributions become important at lower values of D_x, as the crossover to decreasing Néel temperatures at smaller D_x cannot be captured in this order of perturbation theory.

APPENDIX D: BRILLOUIN-WIGNER PERTURBATION THEORY

Here we detail the Brillouin-Wigner perturbation theory [48–50] that we used to derive an effective Hamiltonian in the Ising limit $J \ll D_x$ of the easy-axis Hamiltonian H_{EA}. In this Appendix we work in the S^z basis, and therefore we first rotate the Hamiltonian such that the easy-axis anisotropy aligns in the spin-Z direction. Expressing the rotated Hamiltonian in units of the easy-axis anisotropy D_x, we obtain

$$\tilde{H} = \underbrace{\frac{J}{D_x}\sum_{\langle i,j\rangle} \lambda\left(S_i^x S_j^x + S_i^y S_j^y\right) + S_i^z S_j^z}_{\text{Perturbation } V \text{ with } J/D_x \ll 1} - \underbrace{\sum_i S_i^z S_i^z}_{H^{(0)}}. \qquad \text{(D1)}$$

The energy spectrum of the unperturbed part $H^{(0)}$ is given by the number of $|0\rangle$ states N_0 as $E^{(0)} = -(N - N_0)$. Therefore, the subspaces of the Hilbert space with different number of $|0\rangle$ states N_0 are well separated compared to $J/D_x \ll 1$. In the Ising limit $J/D_x \to 0$, the lowest energy subspace has $N_0 = 0$. We thus divide the Hilbert space into the subspace with $N_0 = 0$ (subspace 1) and $N_0 \geqslant 1$ (subspace 2). The Schrödinger equation in this notation is given by

$$\begin{pmatrix} H_{11}^{(0)} + V_{11} & V_{12} \\ V_{21} & H_{22}^{(0)} + V_{22} \end{pmatrix} \begin{pmatrix} \psi_1 \\ \psi_2 \end{pmatrix} = E \begin{pmatrix} \psi_1 \\ \psi_2 \end{pmatrix}, \qquad \text{(D2)}$$

where $H_{ii} = H_{ii}^{(0)} + V_{ii}$ describe the Hamiltonians in subspace i and V_{12} and V_{21} are perturbations that couple the subspaces 1 and 2. This gives the two equations

$$H_{11}\psi_1 + V_{12}\psi_2 = E\,\psi_1, \qquad \text{(D3)}$$

$$V_{21}\psi_1 + H_{22}\psi_2 = E\psi_2. \qquad \text{(D4)}$$

To obtain an effective theory in subspace 1 we can insert the second equation in to the first and get

$$H_{11}^{\text{eff}} = H_{11}^{(0)} + V_{11} + V_{12}\frac{1}{E - H_{22}^{(0)} - V_{22}}V_{21}. \tag{D5}$$

The energy dependence of the Hamiltonian H_{11}^{eff} can be eliminated by expanding the energy $E = \sum_{k=0}^{\infty} E^{(k)}$ with $E^{(k)} \propto O[(J/D_x)^k]$. Using the identity

$$\frac{1}{A-B} = \sum_{k=0}^{\infty}\left(\frac{1}{A}B\right)^k\frac{1}{A}, \tag{D6}$$

with $A = E^{(0)} - H_{22}^{(0)}$ and $B = V_{22} - \sum_{k=1}^{\infty} E^{(k)}$ then yields the general form

$$\begin{aligned} H_{11}^{\text{eff}} &= H_{11}^{(0)} + V_{11} \\ &\quad + \sum_{l=0}^{\infty} V_{12}\left[\frac{1}{E^{(0)} - H_{22}^{(0)}}\left(V_{22} - \sum_{k=1}^{\infty} E^{(k)}\right)\right]^l \\ &\quad \times \frac{1}{E^{(0)} - H_{22}^{(0)}}V_{21}. \end{aligned} \tag{D7}$$

Therefore, the effective Hamiltonian up to second order is given by

$$H_{11}^{\text{eff}} = H_{11}^{(0)} + V_{11} + V_{12}\frac{1}{E^{(0)} - H_{22}^{(0)}}V_{21} + O\left[\left(\frac{J}{D_x}\right)^3\right]. \tag{D8}$$

The first-order correction V_{11} is given by

$$V_{11} = \frac{J}{D_x}\sum_{\langle i,j\rangle} P_1\left(S_i^z S_j^z\right)P_1, \tag{D9}$$

where P_1 is a projector onto the subspace 1. This can be expressed using classical Ising spins $\sigma_i = \pm 1$, such that $V_{11} = (J/D_x)\sum_{\langle i,j\rangle}\sigma_i\sigma_j$. The off-diagonal part of the perturbation V_{12}, which couples the subspaces 1 and 2, is given by

$$V_{21} = \sum_{\langle i,j\rangle} P_2\frac{J}{D_x}\frac{\lambda}{2}(S_i^+S_j^- + S_i^-S_j^+)P_1, \tag{D10}$$

and V_{12} analogously with just the order of the projectors changed. This yields for the second-order correction

$$\begin{aligned} &V_{12}\frac{1}{E^{(0)} - H_{22}^{(0)}}V_{21} \\ &= P_1\sum_{\langle m,n\rangle}\sum_{\langle i,j\rangle}\left(\frac{J}{D_x}\right)^2\frac{\lambda^2}{4}\frac{1}{-N - \left(-\sum_k S_k^z S_k^z\right)} \\ &\quad \times (S_m^+S_n^- + S_m^-S_n^+)(S_i^+S_j^- + S_i^-S_j^+)P_1. \end{aligned} \tag{D11}$$

Each virtual bond state that is created in subspace 2 has to be acted on again to get back to subspace 1, thus yielding $\langle m,n\rangle = \langle i,j\rangle$. For each bond state $|\pm1,\mp1\rangle$, the action of the operators creates the virtual state $|0,0\rangle$ and act on it again, so we obtain the processes

$$|\pm1,\mp1\rangle \to |0,0\rangle \begin{array}{l}\nearrow |\pm1,\mp1\rangle \\ \searrow |\mp1,\pm1\rangle.\end{array} \tag{D12}$$

If the bond states in subspace 1 are parallel $|\pm1,\pm1\rangle$ the action of the operators is 0. Therefore, the virtual state differs for each bond by exactly two $|0\rangle$ states, so that

$$\frac{1}{E^{(0)} - H_{22}^{(0)}} = \frac{1}{-N - [-(N-2)]} = -\frac{1}{2}. \tag{D13}$$

We thus obtain for the second-order correction

$$H_{11}^{(2)} = -\frac{\lambda^2}{8}\left(\frac{J}{D_x}\right)^2 P_1(V_{\text{diag}} + V_{\text{offdiag}})P_1, \tag{D14}$$

where we introduced the off-diagonal part

$$V_{\text{off-diag}} = \sum_{\langle i,j\rangle}(S_i^+)^2(S_j^-)^2 + (S_i^-)^2(S_j^+)^2, \tag{D15}$$

and the diagonal part

$$V_{\text{diag}} = \sum_{\langle i,j\rangle} S_i^-S_i^+S_j^+S_j^- + S_i^+S_i^-S_j^-S_j^+. \tag{D16}$$

We now consider V_{diag} and $V_{\text{off-diag}}$ in more detail. Both operators can be expressed in terms of spin-1/2 degrees of freedom. First, we examine V_{diag}, which can be expressed as

$$\begin{aligned} V_{\text{diag}} &= 2\sum_{\langle i,j\rangle}\delta_{\sigma_i,\sigma_j} - \sigma_i\sigma_j = 2\sum_{\langle i,j\rangle}\frac{1}{2}(\sigma_i\sigma_j + 1) - \sigma_i\sigma_j \\ &= N_b - 4\sum_{\langle i,j\rangle} S_i^z S_j^z, \end{aligned} \tag{D17}$$

where $\sigma_i = \pm 1$ are as previously introduced classical Ising spins, S_i^z are spin-1/2 variables, and N_b is the number of bonds on the lattice. Turning our attention to the off-diagonal part, we can express it by spin-1/2 operators as follows:

$$V_{\text{off-diag}} = 2\sum_{\langle i,j\rangle}(S_i^+S_j^- + S_i^-S_j^+). \tag{D18}$$

Previously we saw that the first-order correction V_{11} is a classical Ising model with coupling J/D_x. This can be expressed in terms of spin-1/2 variables as well, such that $V_{11} = (4J/D_x)\sum_{\langle i,j\rangle} S_i^z S_j^z$.

Finally, taking into account the first- and second-order corrections and expressing the Hamiltonian in its original units, we obtain the effective spin-1/2 Hamiltonian in the subspace 1,

$$H_{11}^{\text{eff}} = J\sum_{\langle i,j\rangle} -\frac{\lambda_{\text{eff}}}{2}(S_i^+S_j^- + S_i^-S_j^+) + \Delta S_i^z S_j^z, \tag{D19}$$

where

$$\lambda_{\text{eff}} = \frac{\lambda^2}{2}\frac{J}{D_x}, \quad \Delta = \left(4 + \frac{\lambda^2}{2}\frac{J}{D_x}\right). \tag{D20}$$

In the large D_x limit, the easy-axis Hamiltonian can therefore be described by an effective spin-1/2 XXZ model, where in the limit $J/D_x \to 0$, irrespective of the value of λ, the Ising model is obtained exactly.

[1] V. L. Berezinskii, Zh. Eksp. Theor. Fiz. **59**, 907 (1970) [Sov. Phys.-JETP **32**, 493 (1970)].
[2] J. M. Kosterlitz and D. J. Thouless, J. Phys. C **6**, 1181 (1973).
[3] J. Kosterlitz, J. Phys. C **7**, 1046 (1974).
[4] D. Opherden, N. Nizar, K. Richardson, J. C. Monroe, M. M. Turnbull, M. Polson, S. Vela, W. J. A. Blackmore, P. A. Goddard, J. Singleton, E. S. Choi, F. Xiao, R. C. Williams, T. Lancaster, F. L. Pratt, S. J. Blundell, Y. Skourski, M. Uhlarz, A. N. Ponomaryov, S. A. Zvyagin *et al.*, Phys. Rev. B **102**, 064431 (2020).
[5] U. Tutsch, B. Wolf, S. Wessel, L. Postulka, Y. Tsui, H. O. Jeschke, I. Opahle, T. Saha-Dasgupta, R. Valentí, A. Brühl, K. Remović-Langer, T. Kretz, H.-W. Lerner, M. Wagner, and M. Lang, Nat. Commun. **5**, 5169 (2014).
[6] Z. Hu, Z. Ma, Y.-D. Liao, H. Li, C. Ma, Y. Cui, Y. Shangguan, Z. Huang, Y. Qi, W. Li, Z. Y. Meng, J. Wen, and W. Yu, Nat. Commun. **11**, 5631 (2020).
[7] Y. Shen, C. Liu, Y. Qin, S. Shen, Y.-D. Li, R. Bewley, A. Schneidewind, G. Chen, and J. Zhao, Nat. Commun. **10**, 1 (2019).
[8] H. Li, Y. Da Liao, B.-B. Chen, X.-T. Zeng, X.-L. Sheng, Y. Qi, Z. Y. Meng, and W. Li, Nat. Commun. **11**, 1111 (2020).
[9] Y. Li, S. Bachus, H. Deng, W. Schmidt, H. Thoma, V. Hutanu, Y. Tokiwa, A. A. Tsirlin, and P. Gegenwart, Phys. Rev. X **10**, 011007 (2020).
[10] A. Taroni, S. T. Bramwell, and P. C. Holdsworth, J. Phys.: Condens. Matter **20**, 275233 (2008).
[11] N. Rogado, Q. Huang, J. W. Lynn, A. P. Ramirez, D. Huse, and R. J. Cava, Phys. Rev. B **65**, 144443 (2002).
[12] E. S. Klyushina, B. Lake, A. T. M. N. Islam, J. T. Park, A. Schneidewind, T. Guidi, E. A. Goremychkin, B. Klemke, and M. Månsson, Phys. Rev. B **96**, 214428 (2017).
[13] A. Cuccoli, T. Roscilde, V. Tognetti, R. Vaia, and P. Verrucchi, Phys. Rev. B **67**, 104414 (2003).
[14] E. S. Klyushina, J. Reuther, L. Weber, A. T. M. N. Islam, J. S. Lord, B. Klemke, M. Månsson, S. Wessel, and B. Lake, Phys. Rev. B **104**, 064402 (2021).
[15] J. V. José, L. P. Kadanoff, S. Kirkpatrick, and D. R. Nelson, Phys. Rev. B **16**, 1217 (1977).
[16] C. M. Lapilli, P. Pfeifer, and C. Wexler, Phys. Rev. Lett. **96**, 140603 (2006).
[17] A. W. Sandvik and J. Kurkijärvi, Phys. Rev. B **43**, 5950 (1991).
[18] A. W. Sandvik, Phys. Rev. B **59**, R14157 (1999).
[19] O. F. Syljuåsen and A. W. Sandvik, Phys. Rev. E **66**, 046701 (2002).
[20] D. R. Nelson and J. M. Kosterlitz, Phys. Rev. Lett. **39**, 1201 (1977).
[21] E. L. Pollock and D. M. Ceperley, Phys. Rev. B **36**, 8343 (1987).
[22] A. W. Sandvik, Phys. Rev. B **56**, 11678 (1997).
[23] K. Harada and N. Kawashima, J. Phys. Soc. Jpn. **67**, 2768 (1998).
[24] H. Weber and P. Minnhagen, Phys. Rev. B **37**, 5986 (1988).
[25] D. J. Amit, Y. Y. Goldschmidt, and S. Grinstein, J. Phys. A **13**, 585 (1980).
[26] A. W. Sandvik, AIP Conf. Proc. **1297**, 135 (2010).
[27] L. Ornstein and F. Zernike, Proc. K. Ned. Akad. Wet. Ser. B **17**, 793 (1914).
[28] J. Q. Liu, F.-Y. Li, G. Chen, and Z. Wang, Phys. Rev. Research **2**, 033260 (2020).
[29] Z. Zhang, K. Wierschem, I. Yap, Y. Kato, C. D. Batista, and P. Sengupta, Phys. Rev. B **87**, 174405 (2013).
[30] S. Hikami and T. Tsuneto, Prog. Theor. Phys. **63**, 387 (1980).
[31] V. Y. Irkhin and A. A. Katanin, Phys. Rev. B **60**, 2990 (1999).
[32] A. Cuccoli, T. Roscilde, R. Vaia, and P. Verrucchi, Phys. Rev. Lett. **90**, 167205 (2003).
[33] M. E. Fisher and R. J. Burford, Phys. Rev. **156**, 583 (1967).
[34] K. Binder, Phys. Rev. Lett. **47**, 693 (1981).
[35] K. Binder and D. P. Landau, Phys. Rev. B **30**, 1477 (1984).
[36] W. Selke and L. Shchur, J. Phys. A **38**, L739 (2005).
[37] G. Kamieniarz and H. Blote, J. Phys. A **26**, 201 (1993).
[38] F. Alet, S. Wessel, and M. Troyer, Phys. Rev. E **71**, 036706 (2005).
[39] B. Josephson, Phys. Lett. **21**, 608 (1966).
[40] M. E. Fisher, M. N. Barber, and D. Jasnow, Phys. Rev. A **8**, 1111 (1973).
[41] M. Troyer, M. Imada, and K. Ueda, J. Phys. Soc. Jpn. **66**, 2957 (1997).
[42] M. Campostrini, M. Hasenbusch, A. Pelissetto, P. Rossi, and E. Vicari, Phys. Rev. B **63**, 214503 (2001).
[43] M. Blume, Phys. Rev. **141**, 517 (1966).
[44] H. Capel, Physica **32**, 966 (1966).
[45] J. Zierenberg, N. G. Fytas, M. Weigel, W. Janke, and A. Malakis, Eur. Phys. J. Spec. Top. **226**, 789 (2017).
[46] R. Houtappel, Physica **16**, 425 (1950).
[47] S. Göttel, S. Andergassen, C. Honerkamp, D. Schuricht, and S. Wessel, Phys. Rev. B **85**, 214406 (2012).
[48] L. Brillouin, J. Phys. Radium **3**, 373 (1932).
[49] E. P. Wigner, Math. u. Naturwiss. Anzeig. d. Ungar. Akad. Wiss. **LIII**, 475 (1935).
[50] A. Messiah, *Quantum Mechanics: Volume II* (North-Holland, Amsterdam, 1962).